Title

Additive Destabilization of Porous Magnesium Borohydride Framework with Core-Shell Structure

Journal

Small, 17(44)

ISSN

1613-6810

Authors

Dun, Chaochao
Jeong, Sohee
Liu, Yi-Sheng
et al.

Publication Date

2021-11-01

DOI

10.1002/smll.202101989

Peer reviewed

Additive Destabilization of Porous Magnesium Borohydride Framework with Core-shell Structure

Chaochao Dun[1,*], Sohee Jeong[1,2*], Yi-sheng Liu[3], Noemi Leick[4], Tracy M. Mattox[1], Jinghua Guo[3], Joo-Won Lee[2], Thomas Gennett[4,5], Vitalie Stavila[6] and Jeffrey J. Urban[1§]

[1] The Molecular Foundry, Lawrence Berkeley National Laboratory, Berkeley, CA 94720, United States

[2] Materials Architecturing Research Center, Korea Institute of Science and Technology, Seoul, 02792, South Korea

[3] Advanced Light Source, Lawrence Berkeley National Laboratory, Berkeley, CA 94720, United States

[4] National Renewable Energy Laboratory, Golden, CO 80401, United States

[5] Chemistry Department, Colorado School of Mines, 1012 14th Street, Golden, CO 80401, USA

[6] Sandia National Laboratories, Livermore, CA 94551, United States

[§]Corresponding author: jjurban@lbl.gov

Abstract

Design of interfaces with thermodynamic and kinetic specificity is of great importance for hydrogen storage from both an applied and fundamental perspective. Here, in order to destabilize the metal hydride and protect the dehydrogenated products from oxidizing, a unique core-shell structure of porous $Mg(BH_4)_2$-based framework with a thin layer (no more than 5 nm) of $MgCl_2$ additives on the surface, has been proposed and synthesized via a wet-chemical method. The local structure and electronic state of the present complex system were systematically investigated to understand the correlation between the distribution of additives and dehydrogenation property of $Mg(BH_4)_2$. A significant improvement was achieved for hydrogen desorption with chlorides: initial hydrogen release from $MgCl_2$ decorated γ-phase $Mg(BH_4)_2$ particles commences at 100 °C and reaches a maximum of 9.4 wt% at 385 °C. Besides the decreased decomposition temperature, an activation barrier about 76.4 kJ/mol lower than that of

$Mg(BH_4)_2$ without $MgCl_2$ was obtained. Moreover, $MgCl_2$ decoration can also prevent the whole decomposed system (both Mg- and B- elements) from oxidizing, which is a necessary condition to reversibility.

Introduction

Hydrogen is an appealing alternative carbon-free energy carrier to fossil fuels[1]. Traditionally, hydrogen storage has been achieved either in pressurized tanks under 700 bar or in cryogenic containers at 20 K to cover the low density of hydrogen gas, but these techniques are associated with energy losses, expensive storage tanks, and have to pass rigorous safety testing, which seriously hinders its on-board applications[2]. Solid-state hydrogen storage methods are recently explored as an attractive alternative[3,4]. Currently, solid-state hydrogen storage of complex hydrides, such as alanates[5–7], amides[8,9], and borohydrides[10,11], has attracted a lot of attention due to their relatively safe chemical structure and exceptional hydrogen storage capacity. Among them, magnesium borohydride ($Mg(BH_4)_2$) is an inexpensive material having ultra-high gravimetric density of hydrogen (14.8 wt%) and theoretical enthalpy value of -40 kJ mol^{-1} for hydrogen release, which induces theoretically suitable hydrogen storage within the moderate temperature range of 20–75 °C.[12] Unfortunately, bulk $Mg(BH_4)_2$ decomposes in several steps, passing through intermediate species like stable $MgB_{12}H_{12}$ phase where the activation energy is as high as 311 ± 20 kJ mol^{-1}, leading to an undesirable decomposition temperature of above 350 °C[13].

Different strategies have been applied over the past years to decrease the activation energies and reduce the decomposition temperatures of metal hydrides, such as adding catalysts and reducing the particle size of the functional materials[14–16]. Notably, nanostructured hydride materials can directly reduce the barrier of reaction pathways for both hydrogen diffusion and mass transport, so their kinetic properties could be tuned independently of their bulk counterparts[17–19]. For example, it has been reported previously that a nano-confinement approach, where Li-N-H particles with a diameter of ~3.2 nm are infiltrated into porous carbon, decreases the decomposition temperature as a result of the increased reaction kinetics[20]. Using a scaffold which can both confine and thermodynamically destabilize the complex metal hydride is

another potential approach[21,22]. Nano-sized $Mg(BH_4)_2$, when confined into silica aerogels, has demonstrated a significant decrease in its decomposition temperature (~ 60 °C) compared with its bulk counterpart (~320 °C) [23]. Alternatively, the use of additives as thermodynamic destabilization to alter the decomposition pathway, therefore reducing the decomposition and dehydrogenation temperature, is regarded as an efficient way in improving the desorption properties of complex hydrides. These additives could include complex metal hydrides, and fluorides[24,25], chlorides[26], transition metals[27], or even metal oxides[28,29]. Nevertheless, although the adoption of catalysts could indeed modify the kinetics of nanoscale metal hydrides to some extent, the improvement is limited by the density of active sites, the selectivity, as well as the sluggish mass transport.

Magnesium borohydride, containing hydrogen-rich molecular $[BH_4]^-$ anions counterbalanced by Mg cations, has a large number of polymorphs with complex structures comprising several hundred atoms in the unit cells. Among which, γ-$Mg(BH_4)_2$ (space group, Id-3a) is an intriguing example of 3D porous networks with high specific surface area and unique porosity. The porous polymorph γ-$Mg(BH_4)_2$ possesses a high surface area (1160 m^2/g) and a low material density (ρ=0.55 g/cm^3), allowing it to physically absorb an additional 0.8 H_2 molecules to the interior of the $Mg(BH_4)_2$ to form γ-$Mg(BH_4)_2 \cdot 0.8H_2$. Inspired by the role of morphology and the destabilizer effect of additives, this work focuses on the design and fabrication of a unique core-shell $MgCl_2$-γ-$Mg(BH_4)_2$ framework based on a one-step synthesis process in a non-coordinating solvent. The unique structure and the electric status were confirmed using powder X-ray diffraction (XRD), wide-angle X-ray scattering (WAXS), Fourier-transform infrared spectroscopy (FTIR), and X-ray absorption spectroscopy (XAS). By incorporating $MgCl_2$ additives onto the surface of the γ-$Mg(BH_4)_2$ particles, we were able to destabilize the local bonds of $[BH_4]^-$, which successfully reduced the onset decomposition temperature of γ-$Mg(BH_4)_2$ to 100°C. The improved thermodynamics and kinetics make the hydrogen desorption of metal hybrids accessible at lower temperatures. Moreover, the introduction of $MgCl_2$ additives prevented the system from oxidation, especially the generation of boron oxide species during the decomposition process, which is key to developing a regenerative material.

Results and Discussion

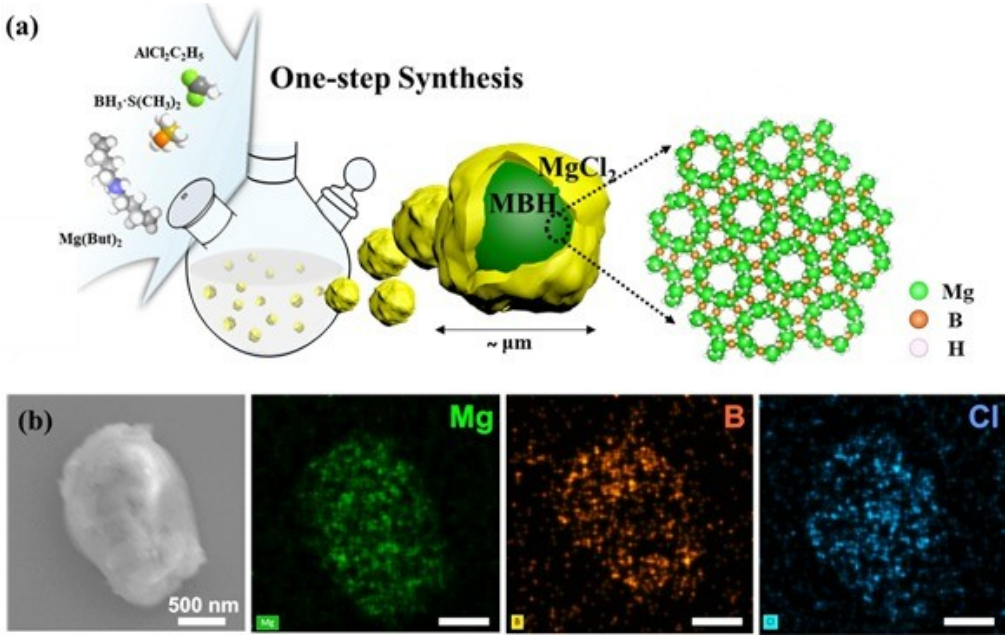

Figure 1. (a) Schematic illustration of the one-step synthetic procedure for the porous $Mg(BH_4)_2$ framework with core-shell structure. (b) SEM and SEM-EDS images for the micron size structure of the composite, with the scale bar represents 500 nm.

Microscale γ-$Mg(BH_4)_2$ materials with and without $MgCl_2$ additives were synthesized in a non-coordinating solvent according to a modified method from previous reports[22,30]. The schematic illustration of the one-step synthesis process of $MgCl_2$-$Mg(BH_4)_2$ was given in **Figure 1(a),** with a more detailed fabrication process given in the experimental section. The typical morphology was revealed by scanning electron microscopy (SEM) with energy dispersive spectroscopy (EDS) mapping. As a comparison, the detailed morphology of $Mg(BH_4)_2$ without $MgCl_2$ was also given in **Figure S1**.

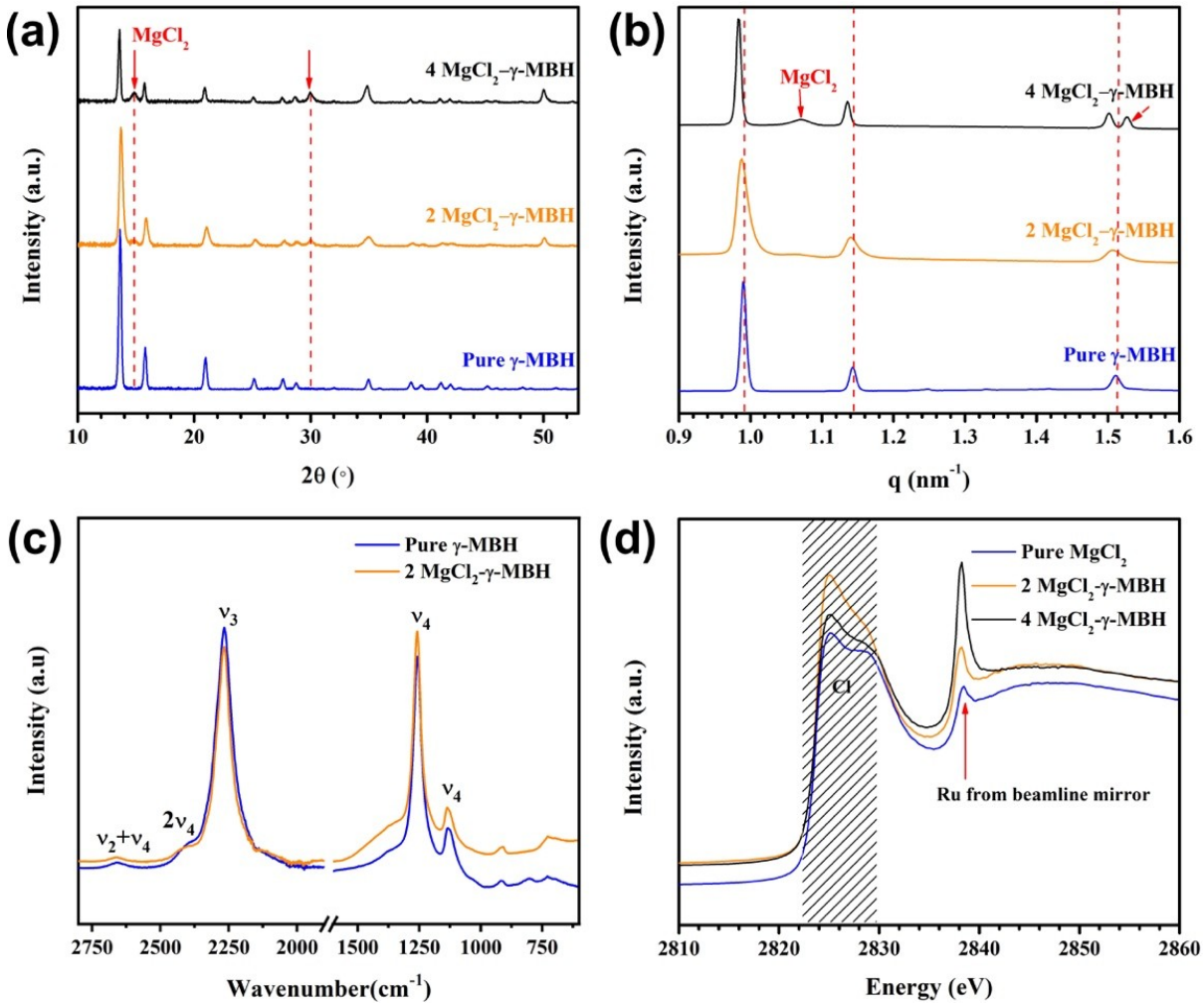

Figure 2. Material characterizations of the porous magnesium borohydride (MBH) framework with and without $MgCl_2$ additives: (a) powder X-ray diffraction (XRD), (b) wide-angle X-ray scattering (WAXS), (c) Fourier-transform infrared spectroscopy measurement, and (d) Cl K-edge X-ray absorption near edge structure (K-XANES) spectra. Here, 2 $MgCl_2$-γ-MBH and 4 $MgCl_2$-γ-MBH means increased amount of additive in the compound, with the detailed stoichiometry summarized in **Table S1**.

The as-synthesized $Mg(BH_4)_2$ were firstly studied by powder XRD in order to determine the crystal structure and the detailed phase polymorph. As can be seen in **Figure 2(a)**, the formation of a single γ-$Mg(BH_4)_2$ phase with high crystallinity was achieved by taking advantage of the rapid drying under vacuum. No trace of α-hexagonal or β-orthorhombic phase can be identified by XRD[31]. Here, the phase behavior of the as-synthesized pure γ-phase is governed by the preferred nucleation kinetics of the metastable β phase above 150 °C, as a result of the energy penalty of directly nucleating the α-phase in the γ-phase[22]. With more concentrated additives,

the presence of solid $MgCl_2$ phase was observed, as marked in **Figure 2(a)**. Careful study of WAXS was carried out to better probe the precise microstructure of γ-$Mg(BH_4)_2$ and the effect of additive introduction, given in **Figure 2(b)**. With $MgCl_2$ additives, the diffraction peaks shifted to lower angles, which confirms the fact that $MgCl_2$ will interrupt the framework of $[BH_4]^-$ and cause lattice strain inside γ-$Mg(BH_4)_2$. This strain was projected to trigger the thermodynamic destabilization of $Mg(BH_4)_2$ and promote the desorption of H_2 at lower temperatures.

Information on the B-H bonding of the as-synthesized $Mg(BH_4)_2$ was also obtained from FTIR measurement (**Figure 2(c)**). As is known, free molecular $[BH_4]^-$ ions have high tetrahedral symmetry and four normal modes of vibrations: symmetric stretching and bending, υ_1 and υ_2; asymmetric stretching and bending, υ_3 and υ_4, respectively. As can be seen**,** typical internal vibration features of the $[BH_4]^-$ group can be readily observed in the spectra before desorption, with the B-H stretching mode centered at 2267 cm^{-1} and the bending modes located at 1259 and 1136 cm^{-1}. Although the B-H stretching and bending regions, as well as the geometries and local environment of $[BH_4]^{-1}$ are very similar in all polymorphs, when combined with XRD/WAXS, it is indicative of a successful synthesis of pure γ-$Mg(BH_4)_2$. With the addition of $MgCl_2$, the principal stretching and bending modes of $[BH_4]^-$ were preserved. However, it is noteworthy that the relative strength of υ_3 and υ_4 were dramatically changed, which might be induced by disorder in the $[BH_4]^-$ structure. A slight red shift around 1136 cm^{-1} was also observed with added $MgCl_2$. Finally, the local electronic and atomic structures of the composite were further revealed by Cl K-edge X-ray absorption near edge structure (K-XANES) spectroscopy, measured in the range of 2810-2860 eV. As seen in **Figure 2(d)**, the feature of Cl K-XANES spectra around 2825 eV is similar to that of the reference $MgCl_2$, which confirms the introduction of $MgCl_2$ and is in agreement with the XRD analysis. Therefore, the interaction of chloride ions is mainly contributed from neighboring Mg atoms in $MgCl_2$-$Mg(BH_4)_2$, which results in the increased bond length and the affected vibrational spectra characterizing the local environment of $[BH_4]^-$.

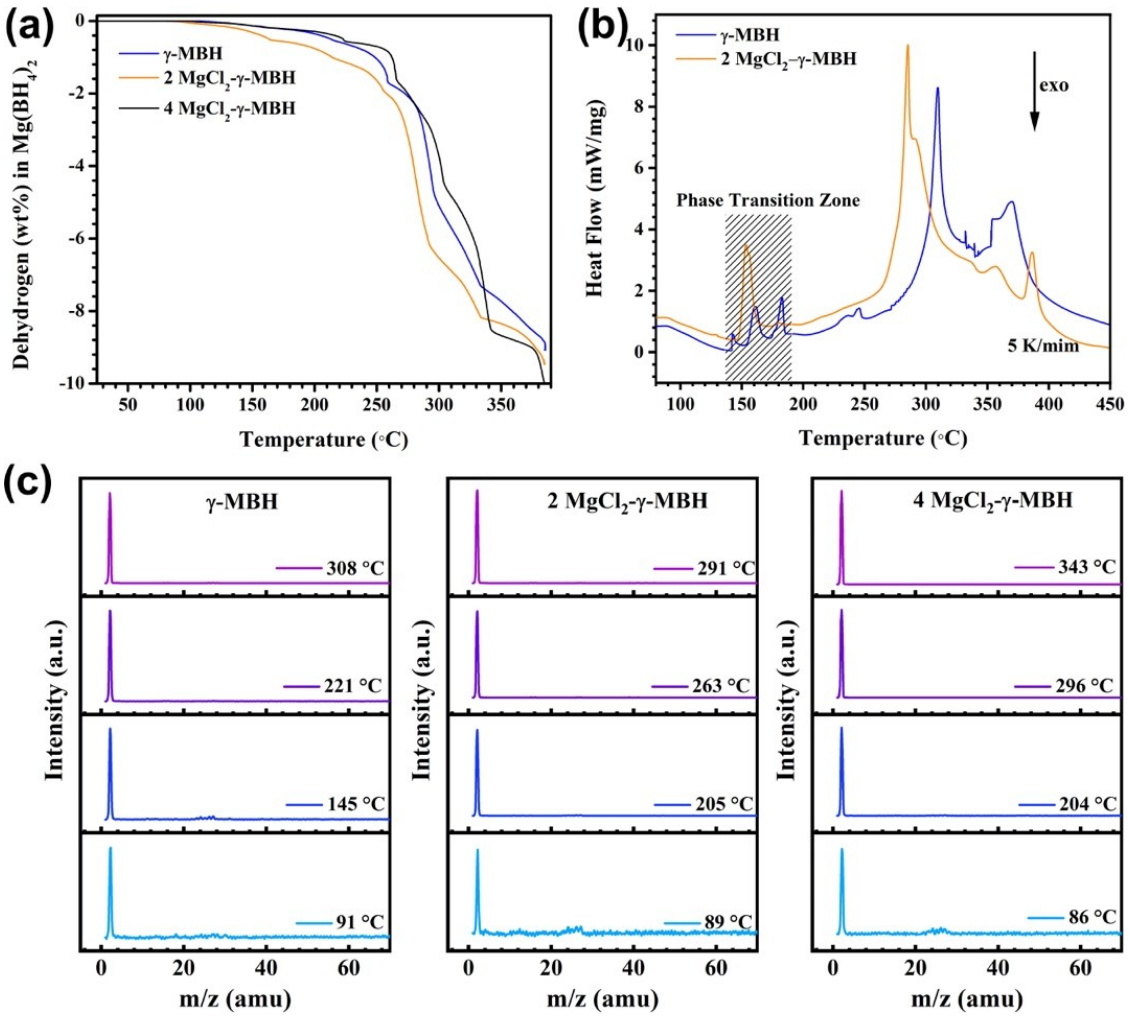

Figure 3. The dehydrogenation kinetic profiles of γ-$Mg(BH_4)_2$ with and without $MgCl_2$ additives: (a) Thermogravimetric analysis (TGA) and (b) the corresponding differential scanning analysis (DSC). (c) Mass spectra of γ-$Mg(BH_4)_2$ with and without $MgCl_2$ additives at varying temperatures until 350 °C.

Beyond the structural characterizations, the dehydrogenation kinetic profiles of γ-$Mg(BH_4)_2$ with and without $MgCl_2$ additives were measured and the representative results are presented in **Figure 3(a)-(b)**. The hydrogen desorption was also measured by a temperature programmed desorption (TPD) system combined with a quadrupole mass spectrometer (QMS) in the temperature range of room temperature to 700°C **(Figure S2**). Here, only hydrogen was detected during the thermal desorption measurement (**Figure 3(c)).** Unlike the α-$Mg(BH_4)_2$ and β-$Mg(BH_4)_2$ showing a one-step weight loss profile (with onset temperatures of 250 and 270 °C, respectively), both changes in the slope of thermogravimetric analysis (TGA) curves and the observed multiple endothermic peaks in the differential scanning analysis (DSA) curves strongly

indicate a multistep dehydriding reaction for porous γ-$Mg(BH_4)_2$. The decomposition temperature was first measured by TGA. As can be seen in **Figure 3(a)**, for a γ-$Mg(BH_4)_2$ without $MgCl_2$ system, the first desorption step occurs at about 140 °C with a release of 2.1 wt% of H_2 at about 260 °C. The second step takes place at 270 °C with the release of another 7.3 wt% of H_2 before 370 °C. The total amount of desorbed hydrogen is about 9.3 wt% at 385 °C. $MgCl_2$ additives have a significant impact on the decomposition temperature, reducing the onset temperature to ~100 °C, with a 3.5 wt% of H_2 content released by 250 ℃. As a result, the present $Mg(BH_4)_2$-based hydride with $MgCl_2$ additives desorbed a total of 9.4 wt% of H_2 at 385 °C. Therefore, including the $MgCl_2$ additives not only results in the hydrogen desorption started at a low temperature (~100 °C) due to the high destabilization effect of $MgCl_2$, but also yields a higher H_2 release at the same temperature range. More concentrated $MgCl_2$ additives will deteriorate this effect and even increase the decomposition temperature because of the passivated surface, as will be discussed in the following.

The corresponding DSC profiles show the phase transformation temperature and the detailed desorption behavior. No exothermic peak originating from the crystallization reaction from amorphous γ-$Mg(BH_4)_2$ was observed (**Figure 3(b)**), which is in agreement with our XRD analysis, i.e. the high crystallization status of the as-fabricated γ-$Mg(BH_4)_2$. Specifically, for γ-$Mg(BH_4)_2$ without $MgCl_2$, the first endothermic event prior to the melting point, located in the range of 150-185 °C, is contributed to the irreversible phase transitions γ→ε→ β' in accordance with a previous study[32]. When combined with TGA analysis, it may be concluded that partial decomposition, although not dramatic, has already occurred together with the formation of ε-$Mg(BH_4)_2$ below 185 °C. The second endothermic event located at 280~330 °C (which peaked at 309°C) corresponds to the amorphous intermediates/melt or the other B-H species like closo-borates, and the main reaction $Mg(BH_4)_2 \rightarrow MgH_2+2B+3H_2$. Beyond 350 °C, $MgH_2 \rightarrow Mg+H_2$ occurs and ultimately results in a maximum H_2 release before 450 °C. On the contrary, the first decomposition of the $MgCl_2$-γ-$Mg(BH_4)_2$ mixture related to the phase change starts around 140-160 °C. Unlike the system without $MgCl_2$, one main sharp peak (at 152 °C) with a small shoulder and one tiny peak (at 180 °C) were observed, which may indicate certain structural disorder induced by the additive. Accordingly, as a competitive destabilizer, $MgCl_2$ additives decrease the γ-$Mg(BH_4)_2$ decomposition temperature starting around 100 °C. This temperature distribution is

consistent with the TGA observations discussed above. Notably, 0.5 wt% of the weight loss in $MgCl_2$-γ-$Mg(BH_4)_2$ that is attributed to the first hydrogen release step. Moreover, the second endothermic event was introduced at a much lower temperature starting around 255 °C. This decomposition temperature is even lower than the nano γ-$Mg(BH_4)_2$ particles captured by reduced graphene oxide (~300 °C) in our previous study[22]. Therefore, $MgCl_2$ additives result in a similar hydrogen desorption behavior but both the desorption temperature and the phase change temperature are dramatically decreased. XRD patterns for $MgCl_2$-γ-$Mg(BH_4)_2$ dehydrogenation at 390 °C was performed to check the final product (**Figure S3**), with the main peaks identified as Mg with a weak peak coming from the small quantities of amorphous MgB_2, which is in agreement with our DSC analysis.

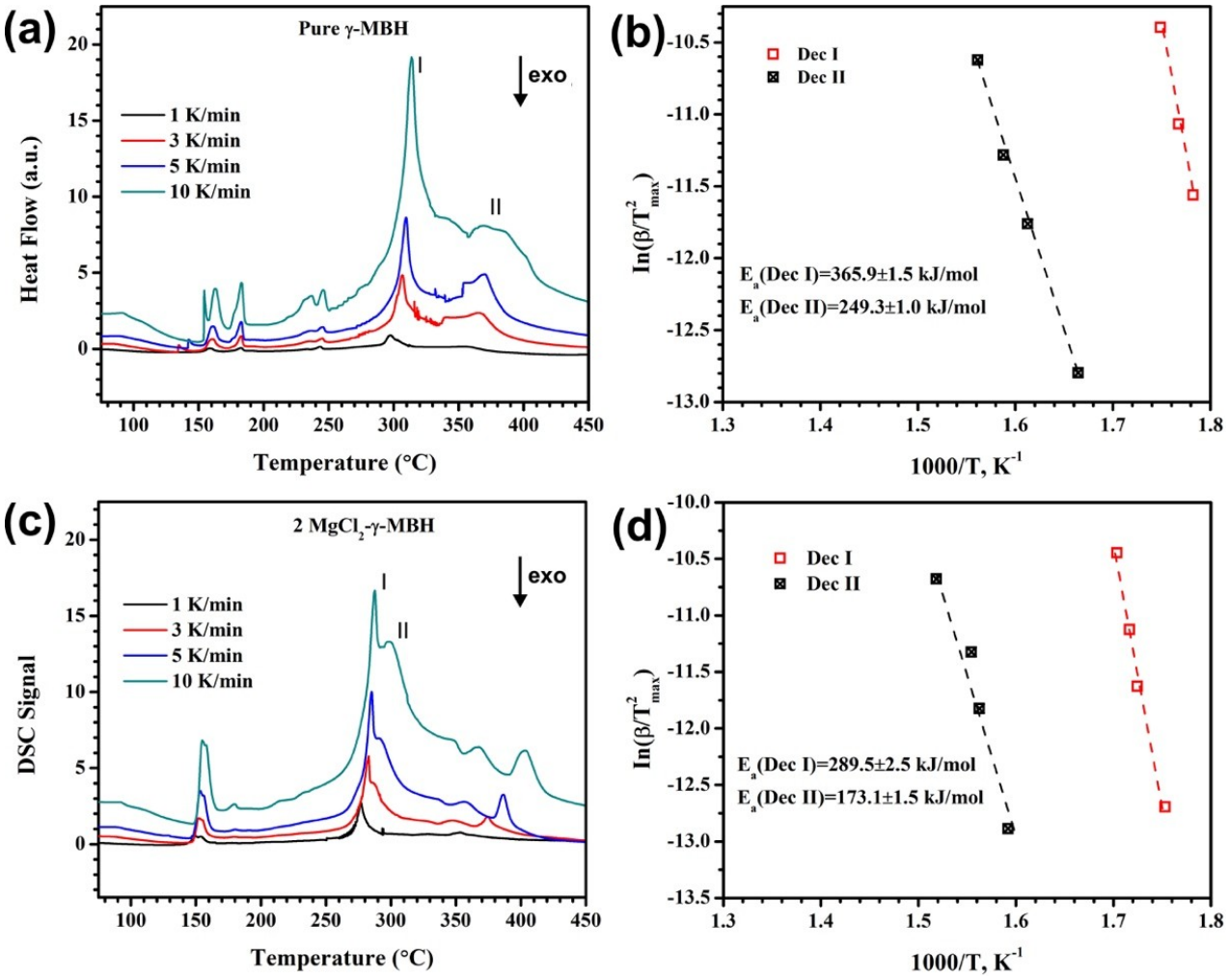

Figure 4. (a) and (c) are the DSC curves with varies temperature increasing rates (1, 3, 5 and 10 K/min) for γ-$Mg(BH_4)_2$ and $MgCl_2$-γ-$Mg(BH_4)_2$ mixture, respectively. (b) and (d) are the corresponding active

energies on the Kissinger method, where β is the heating rate in K/min, and T_m is the temperature at differential heat flow maximum. Here, the labeled Dec I and II represent the two first main decomposition events.

The activation energies were further studied by applying the Kissinger method[33] to the DSC measurements at heating rates of 1, 3, 5 and 10 K/min, respectively. Only two main decomposition events were considered here, marked as I and II in **Figure 4**. T_m is the temperature at differential heat flow maximum. Here, T_{max} for the first decomposition signal shifts from 296 to 314 °C for $Mg(BH_4)_2$ without $MgCl_2$ with increased heating rate, while the corresponding values are decreased to 277 and 287 °C, respectively. As a result, the first decomposition (labeled as I) has the highest kinetic barrier (E_a) that is around 365.9 kJ/mol for γ-$Mg(BH_4)_2$ without $MgCl_2$, and the second one (labeled as II) is around 249.3 kJ/mol. With the addition of $MgCl_2$, the corresponding values decreased to 289.5 and 173.1 kJ/mol, respectively. These values are similar to the previously reported kinetic properties of $Mg(BH_4)_2$ impregnated in activated carbon[13]. Further decreased E_a might be achieved with smaller morphology control of the present composites. The lowered energy barriers were suggested as the reason for the low decomposition temperature, as seen in **Figure (3)**.

In order to develop a better understanding on how $MgCl_2$ additives incorporate into γ-$Mg(BH_4)_2$ and to explore the related mechanism to improve future material design, the local structure of the γ-$Mg(BH_4)_2$ framework was systematically investigated by the decay of total electron yield (TEY) and total yield of fluorescence photons (TFY) through XAS. **Figure (5)** shows the XAS patterns (both TEY and TFY channels) of element Mg at K-edge for $Mg(BH_4)_2$ and $MgCl_2$-γ-$Mg(BH_4)_2$. As is well known, the short escape length of electrons makes the TEY channel surface sensitive with a penetration depth of several nanometers (~5 nm), while the TFY channel is relatively bulk sensitive with a penetration depth of a few micrometers. Therefore, TEY reveals more surface information and TFY reveals more information inside the bulky core. Based on **Figure 5(a)**, the sharp peaks for TEY of the Mg K-edge before desorption (between 1310 and 1320 eV) in $MgCl_2$-γ-$Mg(BH_4)_2$ are likely coming from $MgCl_2$, and the combination of $MgCl_2$ and $Mg(BH_4)_2$. This is in agreement with our XRD and XANES analysis in **Figure 2**. At the same time, all the TFY signals of Mg-K edge are

similar, which shows no traceable sign of $MgCl_2$ for all $MgCl_2$-γ-$Mg(BH_4)_2$ systems (**Figure 5(b)**). Therefore, the present composite is likely to form a core–shell structure, with $MgCl_2$ mainly distributed on the surface of porous γ-$Mg(BH_4)_2$ framework as proposed. After hydrogen desorption, the XAS profiles of all samples are dramatically altered from their initial state, suggesting the local environment of the Mg atom is chemically and structurally different. The TFY for pure MgB_2 and MgO were also measured for comparison. Interestingly, after desorption, the Mg K-edge for 2 $MgCl_2$-γ-$Mg(BH_4)_2$ and $Mg(BH_4)_2$ showed similar behavior, with a strong peak similar to that observed for $Mg[B_mH_n]^{x-}$ in the TEY and TFY (**Figure 5(c)** and **Figure 5(d)**). However, more concentrated $MgCl_2$ will deteriorate this destabilization effect because of the passivated surface as observed here, resulting in undesirable higher decomposition temperature as seen in **Figure 3(a)**. Finally, no noticeable signal from MgO was observed, which is also in agreement with our XRD analysis (**Figure S3**) showing no sign of MgO after desorption.

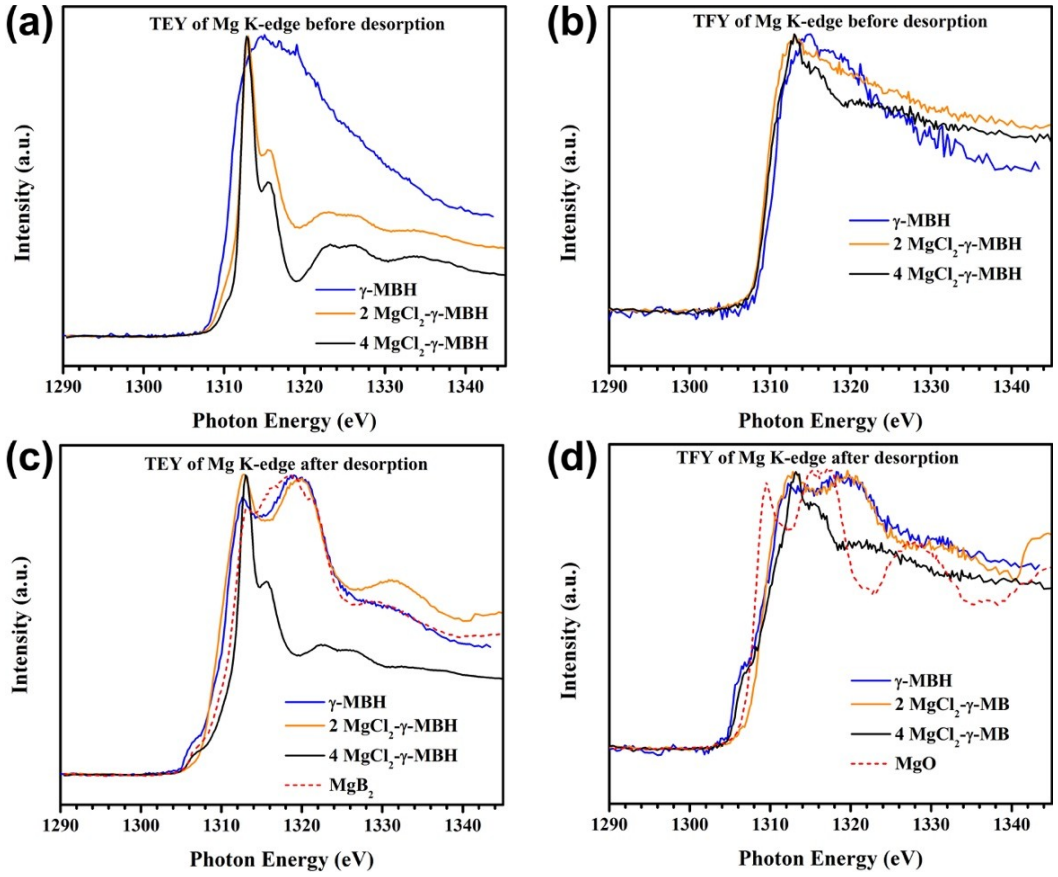

Figure 5. Total electron yield (TEY, penetration depth ~5 nm) and total fluorescence yield (TFY, penetration depth of few micrometers) of X-ray absorption spectroscopy (XAS) of Mg K-edge for $Mg(BH_4)_2$ and $MgCl_2$-γ-$Mg(BH_4)_2$. (a) TEY and (b) TFY of the Mg K-edge before desorption. (c) and (d) are the counterparts after desorption, respectively. The related testing for B K-edge spectra is given in **Figure S4**.

XAS including TEY and TFY of the B K-edge for γ-$Mg(BH_4)_2$ without $MgCl_2$ and $MgCl_2$-γ-$Mg(BH_4)_2$ (as-synthesized and after desorption), were also studied (**Figure S4**). The broad peaks at around 185 eV is related to a generation of borane complexes B_mH_n[34]. It was found out that de-hydrogenated 2 $MgCl_2$-γ-$Mg(BH_4)_2$ in bulk doesn't present the peak corresponding to B_2O_3 (peak around 192.5 eV), which differs from the γ-$Mg(BH_4)_2$ without $MgCl_2$. For $Mg(BH_4)_2$ without $MgCl_2$ after desorption, B_2O_3 signals were observed both near the surface and in the core of the bulk system after desorption. Notably, unlike the decomposition products of $Mg(BH_4)_2$, de-hydrogenated 2$MgCl_2$-γ-$Mg(BH_4)_2$ possesses an amorphous MgB_2. Therefore, we conclude that $MgCl_2$ decoration within the proper amount around 2.0 at% can prevent oxidation of $Mg(BH_4)_2$ system (both Mg- and B) and results in the introduction of borane complexes (B_mH_n) instead of B_2O_3.

Conclusions

To achieve the destabilization of metal-borohydride with better kinetics, a unique γ-$Mg(BH_4)_2$-$MgCl_2$ core-shell structure was proposed for the first time. The additives destabilization of the porous γ-$Mg(BH_4)_2$ framework was systematically explored, including the phase transition, the thermal decomposition temperature, and the related activation energies. Our γ-$Mg(BH_4)_2$ microstructure decorated by $MgCl_2$ on the surface exhibits the lower decomposition temperature than that of γ-$Mg(BH_4)_2$ without $MgCl_2$ and improves the oxidation stability during the dehydrogenation. Subsequently, in the optimal system with atomic ratio of $MgCl_2/Mg(BH_4)_2$ around 0.06, 9.4 wt% of H_2 was released at mild desorption temperature: the initial dehydriding temperature of γ-$Mg(BH_4)_2$ is considerably lowered by the addition of $MgCl_2$ from 150-180 °C down to 100 °C. Data analysis through both the decay of total electron yield and total yield of fluorescence photons through X-ray absorption spectroscopy disclose the contrast between surface and bulk states of the $MgCl_2$-γ-$Mg(BH_4)_2$ system, revealing the precise microstructures

and the local chemical status before and after desorption. This system may serve as a promising strategy for the destabilization and improved oxidation stability in wide range of metal borohydrides.

Experimental Section

Synthesis of $Mg(BH_4)_2$ materials with and without $MgCl_2$ additives

All chemicals were stored in an Ar glovebox when not in use, and all processes were carried out in an Ar glovebox with the exception of centrifugation, which took place using parafilm-sealed centrifuge tubes in open-air. 1M $Mg(C_4H_9)_2$ in heptane and 2M $BH_3{\cdot}S(CH_3)_2$ were purchased from Sigma-Aldrich. 10 mL of $Mg(C_4H_9)_2$ and 20 ml $BH_3{\cdot}S(CH_3)_2$ were uniformly mixed at room temperature. Proper amount of $AlCl_2C_2H_5$ with different volume ratios were used as precursor to provide Cl (2:18 for 2 $MgCl_2$-γ-MBH and 4:16 for 4 $MgCl_2$-γ-MBH). The mixed solution was allowed to stir under Ar overnight. Upon completion of the reaction, the solution was centrifuged (6000 rpm for 20 min), and the supernatant was decanted to remove toluene and excess precursors. The white precipitate was washed three times with anhydrous toluene and subsequently dried under vacuum at 4 Torr for 3 min to produce γ-$Mg(BH_4)_2$. The detailed element ratio is provided in **Table S1** (supporting information).

Characterizations

Powder X-ray diffraction (PXRD, Bruker AXS D8 Discover GADDS X-ray diffractometer using Co K_α radiation at 40 kV/40 mA), and Fourier transform infrared (FTIR) spectra (Agilent Cary-630 spectrometer) were used to confirm the purity of the as-prepared products. The FTIR spectra were acquired with an attenuated total reflectance module containing a diamond crystal, located inside an Argon glovebox to prevent exposure to air. Energy Dispersive X-ray (EDX) spectra were acquired to determine the compositions of all samples based on A Jeol 2100-F 200 kV field-emission analytical transmission electron microscope. The XPS spectra were collected using a K_α X-ray Photoelectron Spectrometer System from Thermo Fisher. A vacuum transfer vessel was used to protect the sample from deliquescence. The spot size of the monochromatic Al X-ray source was fixed at 400 microns and a flood source was adopted for charge neutralization prior to measuring each sample. The XPS data were calibrated to the C 1s signal at 284.8 eV. TGA was measured to clarify the peak temperature of H_2 evolution using a Mettler-Toledo TGA/DSC 1 STARe. 25 mg of sample was placed in pre-weighted aluminum crucibles

inside the glove box, then heated in the TGA using a ramp rate of 5 K min^{-1} under a high purity argon flow of 20 ccm min^{-1}. Gas analysis was performed on a custom-built setup equipped with a turbo molecular pump (Agilent V70D, 75000 rpm) and a Stanford Research Systems CIS 200 closed ion source mass spectrometer with a sample range from 1 to 200 atomic mass units. DSC data was collected using varying heating rates from 2 to 15 K/min, and the activation energy calculated using the Kissinger method from the curves of hydrogen emission recorded by mass spectroscopy. Moreover, the hydrogen desorption was identified by temperature programmed desorption (TPD) system combined with a residual gas analyzer (RGA) in the temperature range of 25 to 700 °C, at a heating rate of 5 °C min^{-1}, utilizing a Digi-Sense temperature controller. In detail, the samples studied for this work were analyzed on a calibrated, custom-built TPD system equipped with a Stanford Research Systems RGA 100, with m/z = 1-100 amu, sampling rate of 4 seconds and 70 eV ionization energy. The quantity of material was adjusted to stay within the calibrated mass spectrometer's linear response region. In a typical analysis, 1-2.5 mg of sample was placed inside a platinum (Pt) foil packet to ensure homogeneous heating of the entire sample during the dehydrogenation process. The sample was then inserted into a quartz tube mounted to the TPD system. All experimental parameters were controlled via a LabView™ interface with the RGA, heating system, and pressure gauges. Typical initial pressures before heating the sample are at 10^{-8} Torr, with a flat baseline, i.e. no water, hydrogen or air signals above background. The data shown was normalized to the mass of the sample weighed before the TPD experiment.

In order to clarify the hydrogen desorption mechanisms of the present system, high-resolution X wide-angle X-ray scattering data were collected at beamline 12.2.2 at the Advanced Light Source (ALS), Lawrence Berkeley National Laboratory. Samples were loaded into 1.0 mm glass capillaries inside a glovebox under an Ar atmosphere and sealed with clay. Analysis of powder X-ray diffraction patterns was performed using TOPAS-Academic v4.1. Soft X-ray absorption spectroscopy measurements at boron and magnesium K-edges were carried out at beamlines 7.3.1 and 8.0.1.4 at the ALS. TEY and TFY signals were recorded simultaneously in XAS experiments, providing surface and bulk sensitive characterizations, respectively. TEY signals were recorded by monitoring the sample drain current, while TFY signals were collected using a channeltron detector. The energy resolutions for the boron and magnesium K-edges were set to

0.1 and 1 eV, respectively. All XAS spectra were normalized to incident photon flux, and the energy calibrated to known reference samples. Samples were prepared in an Ar glovebox (<0.1 ppm of H_2O and O_2) and transferred to the experimental XAS chambers with a UHV-compatible transfer suitcase without exposing to air at any time. XAS spectra were recorded simultaneously with an experimental chamber pressure of $>1 \times 10^{-9}$ Torr.

Acknowledgments

Chaochao Dun and Sohee Jeong contributed equally to this work. This work was supported by the Molecular Foundry and Advanced Light Source at Lawrence Berkeley National Laboratory, and both User Facilities are supported by the Office of Science, Office of Basic Energy Sciences, of the U.S. Department of Energy (DOE) under Contract No. DE-AC02-05CH11231. This work was also supported by Sandia National Laboratories, which is a multimission laboratory managed and operated by National Technology and Engineering Solutions of Sandia, LLC., a wholly owned subsidiary of Honeywell International, Inc., for the U.S. Department of Energy's National Nuclear Security Administration under contract DE-NA-0003525. The authors also gratefully acknowledge research support through the Hydrogen Storage Materials–Advanced Research Consortium (HyMARC), from the U.S. Department of Energy, Office of Energy Efficiency and Renewable Energy, Fuel Cell Technologies Office, under Contract Numbers DE-AC0494AL85000, DE-AC52-07NA27344, and DE-AC36-08GO28308. This research was also supported by National R&D Program through the National Research Foundation of Korea (NRF) funded by Ministry of Science and ICT (2020M3H4A3106354) and the Future Key Technology Program (Project No. 2E31181) funded by the Korea Institute of Science and Technology.

References

[1] L. Schlapbach, A. Züttel, *Nature* **2001**, *414*, 353.

[2] M. B. Ley, L. H. Jepsen, Y. S. Lee, Y. W. Cho, J. M. Bellosta Von Colbe, M. Dornheim, M. Rokni, J. O. Jensen, M. Sloth, Y. Filinchuk, J. E. Jørgensen, F. Besenbacher, T. R. Jensen, *Mater. Today* **2014**, *17*, 122.

[3] K. J. Jeon, H. R. Moon, A. M. Ruminski, B. Jiang, C. Kisielowski, R. Bardhan, J. J. Urban, *Nat. Mater.* **2011**, *10*, 286.

[4] R. Mohtadi, S. I. Orimo, *Nat. Rev. Mater.* **2016**, *2*, 16091.

[5] Y. Pang, Y. Liu, M. Gao, L. Ouyang, J. Liu, H. Wang, M. Zhu, H. Pan, *Nat. Commun.* **2014**, *5*, 3519.

[6] G. Sandrock, K. Gross, G. Thomas, *J. Alloys Compd.* **2002**, *339*, 299.

[7] A. Zaluska, L. Zaluski, *J. Alloys Compd.* **2000**, *298*, 125.

[8] W. I. F. David, M. O. Jones, D. H. Gregory, C. M. Jewell, S. R. Johnson, A. Walton, P. P. Edwards, *J. Am. Chem. Soc.* **2007**, *129*, 1594.

[9] J. W. Makepeace, T. He, C. Weidenthaler, T. R. Jensen, F. Chang, T. Vegge, P. Ngene, Y. Kojima, P. E. de Jongh, P. Chen, W. I. F. David, *Int. J. Hydrogen Energy* **2019**, *44*, 7746.

[10] R. Wu, X. Zhang, Y. Liu, L. Zhang, J. Hu, M. Gao, H. Pan, *Small* **2020**, *16*, 2001963.

[11] M. Paskevicius, L. H. Jepsen, P. Schouwink, R. Černý, D. B. Ravnsbæk, Y. Filinchuk, M. Dornheim, F. Besenbacher, T. R. Jensen, *Chem. Soc. Rev.* **2017**, *46*, 1565.

[12] V. Ozolins, E. H. Majzoub, C. Wolverton, *J. Am. Chem. Soc.* **2009**, *131*, 230.

[13] M. Fichtner, Z. Zhao-karger, J. Hu, A. Roth, P. Weidler, *Nanotechnology* **2009**, *20*, 204029.

[14] V. A. Kuznetsov, T. N. Dymova, *Bull. Acad. Sci. USSR, Div. Chem. Sci.* **1971**, *20*, 204.

[15] R. Mohtadi, M. Matsui, T. S. Arthur, S. J. Hwang, *Angew. Chemie - Int. Ed.* **2012**, *51*, 9780.

[16] H. Zhang, G. Xia, J. Zhang, D. Sun, Z. Guo, X. Yu, *Adv. Energy Mater.* **2018**, *8*, 1702975.

[17] C. P. Balde, B. P. C. Hereijgers, J. H. Bitter, K. P. De Jong, *J. Am. Chem. Soc.* **2008**, *130*, 6761.

[18] G. Xia, D. Li, X. Chen, Y. Tan, Z. Tang, Z. Guo, H. Liu, Z. Liu, X. Yu, *Adv. Mater.* **2013**, *25*, 6238.

[19] Y. Luo, Q. Wang, J. Li, F. Xu, L. Sun, Y. Zou, H. Chu, B. Li, K. Zhang, *Mater. Today Nano* **2020**, *9*, 100071.

[20] B. C. Wood, V. Stavila, N. Poonyayant, T. W. Heo, K. G. Ray, L. E. Klebanoff, T. J. Udovic, J. R. I. Lee, N. Angboonpong, J. D. Sugar, P. Pakawatpanurut, *Adv. Mater. Interfaces* **2017**, *4*, 1600803.

[21] E. S. Cho, A. M. Ruminski, S. Aloni, Y. S. Liu, J. Guo, J. J. Urban, *Nat. Commun.* **2016**, *7*, 10804.

[22] S. Jeong, T. W. Heo, J. Oktawiec, R. Shi, S. Kang, J. L. White, A. Schneemann, E. W. Zaia, L. F. Wan, K. G. Ray, Y. S. Liu, V. Stavila, J. Guo, J. R. Long, B. C. Wood, J. J. Urban, *ACS Nano* **2020**, *14*, 1745.

[23] M. Rueda, L. M. Sanz-moral, A. Girella, *Int. J. Hydrogen Energy* **2016**, *41*, 15245.

[24] Z. G. Zhang, H. Wang, J. W. Liu, M. Zhu, *Thermochim. Acta* **2013**, *560*, 82.

[25] A. Al-Kukhun, H. T. Hwang, A. Varma, *Int. J. Hydrogen Energy* **2012**, *37*, 17671.

[26] E. G. Bardají, N. Hanada, O. Zabara, M. Fichtner, *Int. J. Hydrogen Energy* **2011**, *36*, 12313.
[27] Z. Huang, Y. Wang, D. Wang, F. Yang, Z. Wu, L. Wu, Z. Zhang, *Phys. Chem. Chem. Phys.* **2019**, *21*, 11226.
[28] O. Zavorotynska, I. Saldan, S. Hino, T. D. Humphries, S. Deledda, B. C. Hauback, *J. Mater. Chem. A* **2015**, *3*, 6592.
[29] N. Leick, N. A. Strange, A. Schneemann, V. Stavila, K. Gross, N. Washton, A. Settle, M. B. Martinez, T. Gennett, S. T. Christensen, *ACS Appl. Energy Mater.* **2021**, *4*, 1150.
[30] S. Jeong, P. J. Milner, L. F. Wan, Y. Liu, J. Oktawiec, E. W. Zaia, A. C. Forse, N. Leick, T. Gennett, J. Guo, D. Prendergast, J. R. Long, J. J. Urban, *Adv. Mater.* **2019**, *31*, 1904252.
[31] M. Paskevicius, M. P. Pitt, C. J. Webb, D. A. Sheppard, U. Filsø, E. M. Gray, C. E. Buckley, *J. Phys. Chem. C* **2012**, *116*, 15231.
[32] O. Zavorotynska, A. El-Kharbachi, S. Deledda, B. C. Hauback, *Int. J. Hydrogen Energy* **2016**, *41*, 14387.
[33] H. E. Kissinger, *Anal. Chem.* **1957**, *29*, 1702.
[34] R. J. Newhouse, V. Stavila, S. J. Hwang, L. E. Klebanoff, J. Z. Zhang, *J. Phys. Chem. C* **2010**, *114*, 5224.